Ultramicroscopy 231 (2021) 113270

Contents lists available at ScienceDirect

Ultramicroscopy

journal homepage: www.elsevier.com/locate/ultramic

Combining quantitative ADF STEM with SiN_x membrane-based MEMS devices: A simulation study with Pt nanoparticles

Katherine E. MacArthur [a,*], Antoine Clement [a,b], Marc Heggen [a], Rafal E. Dunin-Borkowski [a]

[a] Ernst Ruska-Centre for Microscopy and Spectroscopy with Electrons and Peter Grünberg Institute, Forschungszentrum Jülich, 52425 Jülich, Germany
[b] Ecole Nationale Supérieure des Mines de Nancy, Campus Artem, BP 14234, 92 rue du Sergent Blandan, 54042 Nancy cedex, France

ARTICLE INFO

Keywords:
ADF STEM
Quantification
In-situ
Nanoparticles
Atom Counting
Cross Sections

ABSTRACT

Computer simulations are used to assess the influence of a 20-nm-thick SiN_x membrane on the quantification of atomic-resolution annular dark-field (ADF) scanning transmission electron microscopy images of Pt nanoparticles. The discussions include the effect of different nanoparticle/membrane arrangements, accelerating voltage, nanoparticle thickness and the presence of adjacent atomic columns on the accuracy with which the number of Pt atoms in each atom column can be counted. The results, which are based on the use of ADF scattering cross-sections, show that an accuracy of better than a single atom is attainable at 200 and 300 kV. At 80kV, the scattering in a typical SiN_x membrane is sufficiently strong that the best possible atom counting accuracy is reduced to +/- 2 atoms. The implications of the work for quantitative studies of Pt nanoparticles imaged through SiN_x membranes are discussed.

1. Introduction

A full understanding of the relationship between the structure and performance of catalyst nanoparticles requires local atomic-resolution characterisation of their structure and composition, in particular at their surfaces. An important tool to obtain such information is the transmission electron microscope (TEM). However, if characterisation is restricted to *post mortem* analyses in vacuum, before and after a reaction occurs, then information about structural evolution that takes place under realistic operational conditions may not be captured [1,2]. Two approaches can be used to study the evolution of catalyst particles at elevated pressure and temperature on the atomic scale. The first approach makes use of microelectromechanical systems (MEMS) technology to create small reaction chambers (or E-cells) between SiN_x membranes in dedicated specimen holders. The electron-transparent SiN_x windows, which are typically 20-30 nm thick, allow reactions to be imaged at pressures that can exceed 1 bar [3]. Such SiN_x membranes contain predominantly Si and N, but have also been shown to contain small amounts of O and Cl, whose concentrations depend on the synthesis method [4]. The second approach involves the use of a differentially-pumped environmental TEM (ETEM) [5] to introduce gas near the sample at a pressure of typically up to ~50 mbar. In the latter case, changes in sample temperature are often also introduced using MEMS-based holders. It is clear that the use of SiN_x membranes affects the spatial resolution of images of catalyst particles. However, their influence on quantitative measurements has yet to be investigated systematically.

Even though it is important to understand the structural evolution and deactivation of catalysts over time in three dimensions (3D) [1,6], TEM experiments are usually carried out in a single viewing direction, which complicates direct 3D interpretation. It would be highly beneficial to be able to follow dynamic processes such as Ostwald ripening and particle coalescence in 3D and to explore the feasibility of atomic-scale 3D analysis of catalyst nanoparticles using MEMS-based *in situ* holders. 3D information can be obtained tomographically in the TEM by combining information from images recorded at different sample tilt angles. Of particular interest for studies of catalyst nanoparticles is discrete tomography [7–9], as the number of images can be reduced to 15 or fewer. However, the application of tomography during *in situ* experiments is laborious, as the acquisition of a tilt series can be time-consuming and is in many cases impossible due to geometric restrictions. Although fast tomography has been demonstrated by interrupting heating experiments and quenching the sample to room temperature before recording each continuous tilt series of images [10], the use of such an approach is less appropriate for chemical reactions in gas or liquid environments. In addition, it is not possible to remove gas

* Corresponding author.
E-mail address: k.macarthur@fz-juelich.de (K.E. MacArthur).

https://doi.org/10.1016/j.ultramic.2021.113270
Received 8 September 2020; Received in revised form 24 March 2021; Accepted 5 April 2021
Available online 6 April 2021

from a nanoreactor instantaneously.

Quantitative aberration-corrected annular dark-field (ADF) scanning TEM (STEM) can be used to provide 3D information from single images [11–13] on a frame-by-frame basis. This method relies on converting experimental images to an absolute scale by using a detector normalisation method [14,15], so that images can be analysed with reference to the incident beam intensity. In order to perform this calibration, the electron beam is scanned over the ADF STEM detector to record a sensitivity map. The average pixel intensity in the detector map is considered to be 100% of the incident beam intensity. Dividing the experimental images by this value then results in images that can be displayed on an absolute scale as a fraction of the incident beam intensity. However, detector asymmetries should ideally also be taken into account [16–18]. Processing the calibrated images in this way has been used to determine numbers of atoms in individual atomic columns in recorded images [11–13,19–24], as well as local values of sample thickness [25] and composition [26–31]. It should be noted that the measurement of a chosen quantity is often only possible if the other parameter (*e.g.*, composition or thickness) can be measured independently. Data analysis can be performed either by statistical methods [20] or through comparisons with simulations, in particular by using probe-integrated scattering cross sections [32–34], which have been shown to vary little with probe shape, astigmatism and sample tilt. Scattering cross sections can be obtained by simply integrating the STEM image formation equation [35] (Eq. 1.1). The image intensity is a convolution between the object function $O(\boldsymbol{r})$ and the probe function $P(\boldsymbol{r}_0 - \boldsymbol{r})$ according to the expression

$$I(\boldsymbol{r}_0) = \int P(\boldsymbol{r}_0 - \boldsymbol{r}) O(\boldsymbol{r}) d^2\boldsymbol{r}, \tag{1.1}$$

where $I(\boldsymbol{r_0})$ is the intensity as a function of probe position, specified as a fraction of the incident beam intensity. Integration over an atomic column or region of interest that contains a discrete number of pixels is described by Eq. 1.2. A summation over the probe function with respect to all probe positions $\sum_i A_i P(\boldsymbol{r}_0 - \boldsymbol{r})$ is equal to unity, leaving only a dependency of integrated intensity on the object function, according to Eq. 1.3.

$$\sum_i I_i A_i = \int \sum_i A_i P(\boldsymbol{r}_0 - \boldsymbol{r}) O(\boldsymbol{r}) d^2\boldsymbol{r} \tag{1.2}$$

$$A \sum_i I_i = \int O(\boldsymbol{r}) d^2\boldsymbol{r} = \sigma \tag{1.3}$$

Although accurate atom counting requires the use of a minimum electron dose to provide a sufficient signal-to-noise ratio [36], this dose can be accumulated over several frames to reduce beam damage [37]. Jones *et al.* [11] showed that quantitative STEM can be used to study a time series of images of particle damage in the presence of the electron beam. A hybrid method that involves both statistical analysis and image simulations allows atomic columns that have been missed using the statistical method to be recovered from library information [22]. Altantzis *et al.* studied the stabilities of surface facets on Pt nanoparticles in different gas environments [21], while De wael *et al.* extended the statistical analysis approach by making use of additional information from sequentially-recorded images [38]. There is great potential for extending these methods to understand transformations of particle morphologies over the course of catalytic reactions.

Here, we use computer simulations to assess the influence of the presence of a silicon nitride membrane, which can, for example, be used in both an E-Cell and an ETEM (when using a MEMS-based heating holder) and has a typical thickness of 20-30 nm, on the accuracy of ADF STEM image quantification by atom counting. Understanding the detrimental scattering effect of the membrane is an important step towards experimental design for optimising accuracy. We used a faceted Pt nanoparticle as the sample material in our simulations, as it represents a highly relevant catalyst material for many reactions, such as the oxygen reduction reaction (ORR) in fuel cells [39].

The activity of Pt-based catalysts in the ORR has been shown to decrease in the sequence Pt(110) > Pt(111) > Pt(100) [40]. In addition, ad-atoms have been shown to bind to oxygen atoms, thereby reducing the activities of the particles [13]. The analysis of their 3D structure and the application of atom counting to Pt-based catalysts during *in situ* experiments could therefore provide useful information, which may lead to the development of more active and stable catalyst materials.

2. Methods

2.1. Simulation details

Models of amorphous silicon nitride were created using a similar approach to that of Surrey *et al.* [41] by distributing Si and N atoms randomly in the ratio 3:4 with a density of 3.2 g/cm^3 in a volume of 5 × 5 × 20 nm^3. Although this is a simple approximation of an amorphous structure, the structural details of amorphous materials do not normally have a significant influence on image formation [42]. As stated in the introduction, such films have been shown to contain small amounts of Cl (~0.5% relative to Si) [4] and O. While the presence of these impurities has implications for compositional analysis, their effects on quantitative STEM are expected to be negligible. The assumption of a 0.5 at% contamination of both O and Cl would increase the mean atomic number and density by less than 0.1%.

A <110>-oriented nanoparticle comprising 640 Pt atoms assembled in a truncated octahedron with a bulk face centred cubic crystal structure and a lattice constant of 0.392 nm was chosen for study. In order to assess the influence of the presence of stoichiometric Si_3N_4 on the accuracy of the quantitative interpretation of ADF STEM images, a series of simulations was performed for the following configurations (with shorthand labels given in brackets and illustrated in Fig. 1): nanoparticle only (Pt); Si_3N_4 only (Si_3N_4) (not illustrated in Fig. 1); nanoparticle above Si_3N_4 (Pt-Si_3N_4); nanoparticle below Si_3N_4 (Si_3N_4-Pt), nanoparticle below Si_3N_4 with a 2 nm gap (Si_3N_4-Vac-Pt) (not illustrated in Fig. 1); nanoparticle between 20 nm Si_3N_4 layers (Si_3N_4-Pt-Si_3N_4). The simulation with a nanoparticle above Si_3N_4 is representative of an experiment performed on a heating chip. The simulation with a nanoparticle between Si_3N_4 layers is representative of a nanoreactor cell or E-Cell, in this case with a narrow separation between the membranes.

The presence of a gas environment between the membranes was not considered here, as it would increase the time required for the simulations significantly and reduce their general applicability, given the range of gases that can be used. A rough estimate of the contribution of the gas environment is summarised by the following calculations. At a temperature of 800 K and a pressure of 1 bar, a nanoreactor has a typical maximum separation between the SiN_x membranes of ~30 μm due to bulging. The central position on the window is therefore often not used for imaging and a location closer to the edge is preferred. On the assumption that a separation of 15 μm is more realistic during an *in situ* experiment, for a 0.1 nm^2 probe area the electron beam is predicted to interact with 14 molecules of an ideal gas. Although this estimate does not include the effect of beam spreading, only the part of the beam that is directly above and below an atomic column is usually important for ADF quantification. In comparison, an equivalent region of a 20-nm-thick Si_3N_4 membrane used as one chip of a nanoreactor contains 8.2 Si and 10.94 N atoms, while the addition of a 30-nm-thick Si_3N_4 membrane as a second chip increases these numbers to 20.5 Si and 27.35 N atoms, which is almost three times the mass thickness of the gas region (assuming N_2 gas). In order to simulate the gas accurately, the input structure would need to be 250 times thicker than for a single Si_3N_4 membrane, making it computationally too expensive at this time. The 25% contribution to the mass thickness from the gas is a minor contribution to what is already a small effect of the Si_3N_4 membrane.

The simulations described below were carried out for an aberration-

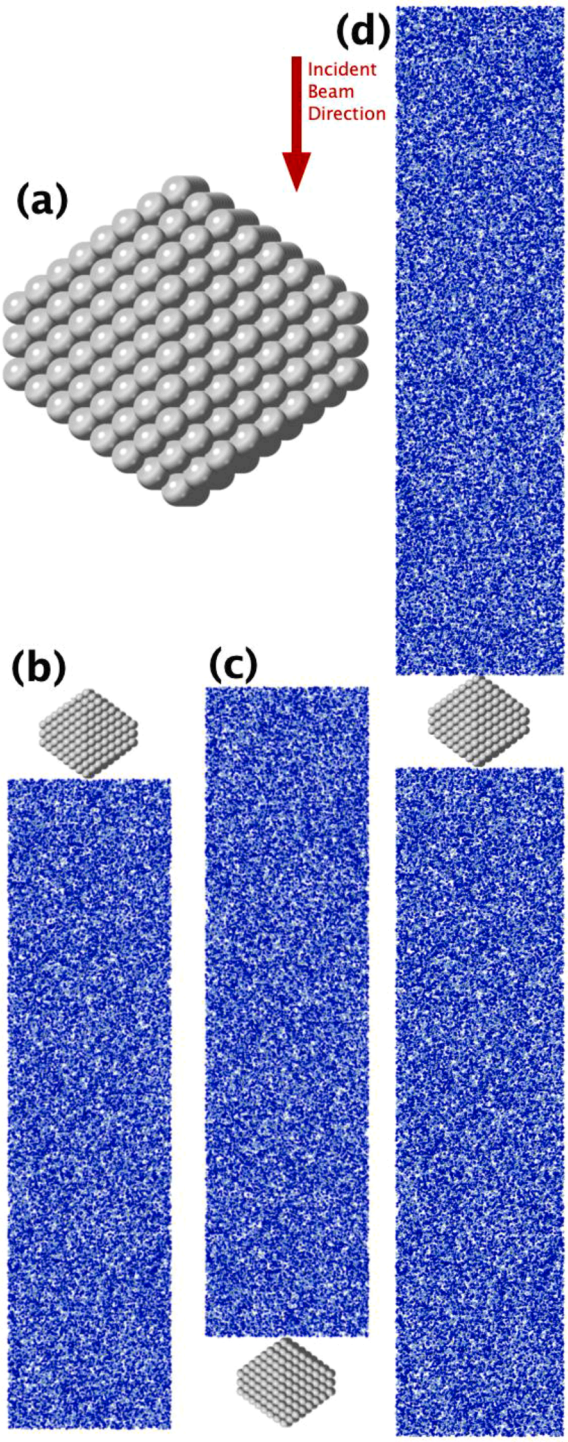

Figure 1. Three-dimensional representations of the structures that were used for the simulations described in this paper. (a) Pt nanoparticle alone; (b) Pt nanoparticle on top of a Si_3N_4 membrane; (c) Pt nanoparticle at the bottom of a Si_3N_4 membrane; (d) Pt nanoparticle sandwiched between Si_3N_4 membranes. The incident electron beam direction is vertically downwards on the page.

corrected STEM using the following parameters: accelerating voltage 80, 200 or 300 kV; convergence semi-angle 25 mrad; high-angle ADF detector collection semi-angle range 70-150 mrad. They were performed using the μstem software (version 5.3_single_precision) with the quantum excitation of phonons (QEP) multislice approach [43] and 'on the fly' potential calculations to reduce memory requirements [44]. Atomic displacements were included based on an Einstein distribution, with mean square displacements of 0.006333 $Å^2$ for Si and N and 0.004864 $Å^2$ for Pt [45]. The defocus plane was set to the top of the Pt nanoparticle, *i.e.*, 0 nm for Pt and Pt-Si_3N_4 and -20 nm for Si_3N_4 -Pt. Whereas 150 slices were used to model each Si_3N_4 membrane, the Pt nanoparticle was sampled more finely at 1 slice per atomic layer, making 19 slices. Simulations of a Pt nanoparticle with one Si_3N_4 membrane therefore contained 169 slices, while those with two membranes contained 319 slices. A series of simulations of a Pt crystal, based on a single unit cell, was also performed to create a comparison library. A <110> orientation was again assumed and the crystal was tiled to achieve a thickness of up to 15 atoms.

2.2. Analysis details

Analysis of the simulation results was carried out using a combination of Atomap and Hyperspy Python libraries [46,47]. These libraries, which were written for the analysis of microscopy data, provide routines for automated peak finding and intensity integration *via* Voronoi cell segmentation [48,49] for each atomic column in an image, as shown in Figs 2 and 3. Multiplication of the resulting values by the corresponding pixel areas converts the integrated intensities into scattering cross sections, which are presented here in units of Mb (megabarns) [32]. Voronoi integration is a robust method of integration for thin samples, even if slight sample mis-tilt leads to movements of atomic column positions [50], as the cells remain almost unchanged [51]. So long as the atomic columns are sufficiently resolved and integrated over completely, the choice of integration method usually does not matter [32]. Two-dimensional Gaussian fitting applied by other researchers would be equally valid, but is in practice more difficult to apply to the analysis of Si_3N_4 images, where no discrete atomic columns are present in the image.

The number of atoms in each atomic column is known from the input structure and is shown in Fig. 2. This knowledge was used to determine how the cross-section changes for a given column thickness as a result of the addition of a Si_3N_4 membrane above and/or below the nanoparticle. Slight variations were seen between atomic columns that had the same thickness but differing neighbouring columns, as a result of the effect of probe tails from the nearby columns [52]. In the simulations of amorphous Si_3N_4, atomic-scale contrast features are visible, even though no systematic alignment of atomic columns is present. The atomic column positions from the Pt-only simulation were therefore used as the basis for segmentation and integration of Voronoi regions on the substrate. This approach provided regions that had the same size and location as those

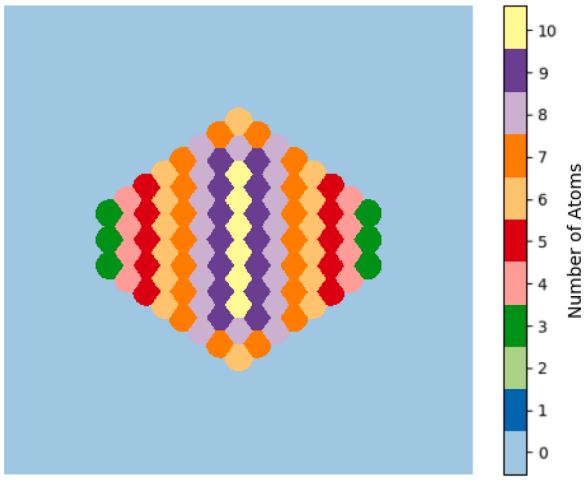

Figure 2. Atom column thickness map denoting the number of atoms in each atomic column in the Pt nanoparticle input structure. The Pt nanoparticle is viewed down the <110> zone axis. The viewing direction is that same as the electron beam direction in Fig. 1.

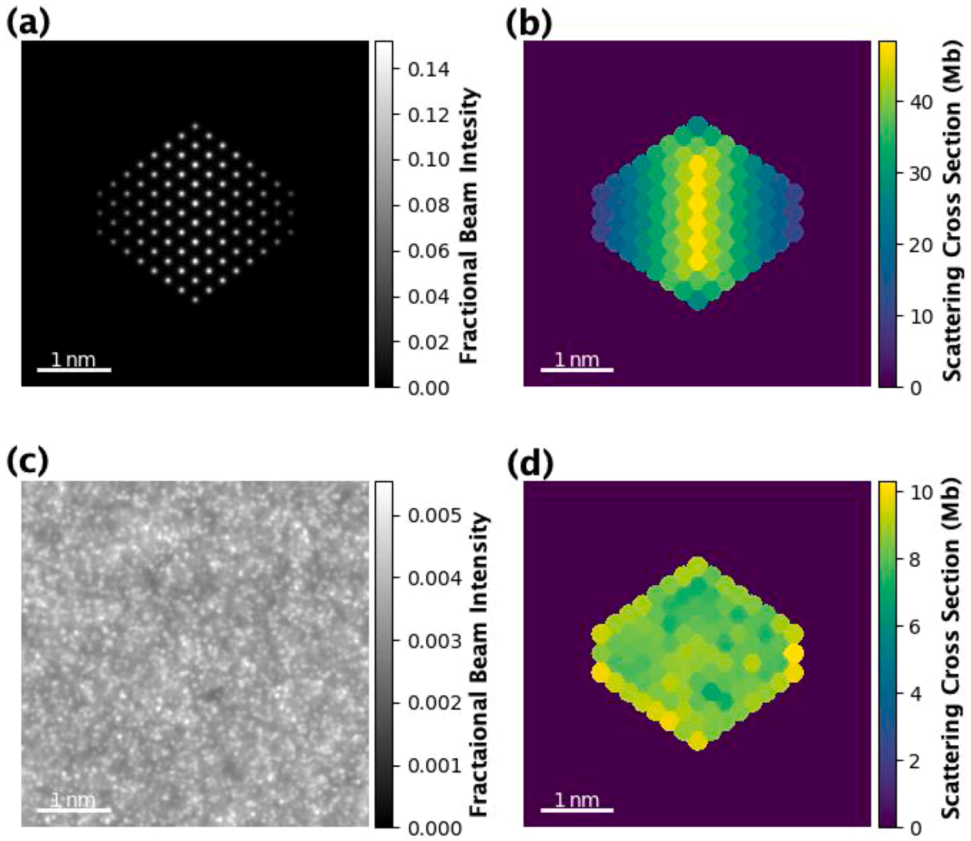

Figure 3. Results of 300 kV simulations: (a) Simulated image of a Pt nanoparticle viewed down the <110> zone axis; (b) Resulting cross-section map; (c) Simulated image of Si_3N_4; (d) Resulting cross-section map obtained by choosing the same integration regions as for the Pt nanoparticle.

in the Pt-only simulation, as shown in Figs 3c and 3d, thereby facilitating easier comparison between all of the calculations. In the graphs of results that are presented below, the analysis steps (integration, subtraction of difference values, *etc.*) were carried out for each atomic column before evaluating averages and standard deviations over all atomic columns of the same thickness, in order to provide an understanding of the accuracy of ADF STEM image quantification.

3. Results and discussion

The main results obtained from the simulations are summarised in Figs 4 and 5. Figure 4 shows scattering cross sections for one 20-nm-thick silicon nitride membrane plotted as a function of location within the image (taken from atomic column assignments) for the three accelerating voltages. Each error bar corresponds to one standard deviation. Figure 5 shows the remaining results sub-divided according to accelerating voltage. For each data point, the average Si_3N_4 intensity has been subtracted to allow a direct comparison with the Pt crystal reference library. The results for the Si_3N_4 membrane (Fig. 4) show a steady average cross-section that is independent of location in the image, as expected for an amorphous sample of constant thickness. It should be noted that the atomic column label values in this plot are not meaningful, as they refer to the Pt nanoparticle. However, the atomic column locations are a reasonable approach for segmenting the intensities across the image. There is an expected increase in integrated intensity for the 3-atom-column regions at the particle surface, where the integration area is slightly inflated due to bowing out of the cells (see Fig. 2). This increase corresponds to an additional 3.5% in the number of pixels present for each outer cell. A slightly higher number of Si and N columns is then included in the integration zone, resulting in an increased intensity. The same integration areas were used for comparing each of the simulation sets. When subtractions and differences were carried out, the same

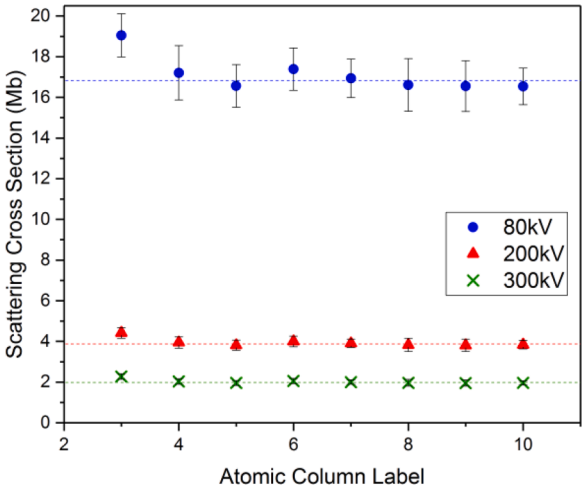

Figure 4. Individual scattering cross sections for a 20-nm-thick silicon nitride film, similar to that shown in Fig. 2d, separated into equivalent atomic columns as for the Pt nanoparticle.

integration size was considered. It has previously been shown that the scattering cross-section is robust to integration area, provided that the 'significant intensity of the column' is included [32]. Figure 5 shows that there is no noticeable effect for the 3-atom columns in the Pt simulations.

For data corresponding to the Pt nanoparticle being located above and/or below the Si_3N_4 membrane, the values in Fig. 4 were subtracted, allowing for a direct comparison with Pt reference values. The resulting integrated intensities match well at 200 and 300 kV. However, at 80 kV

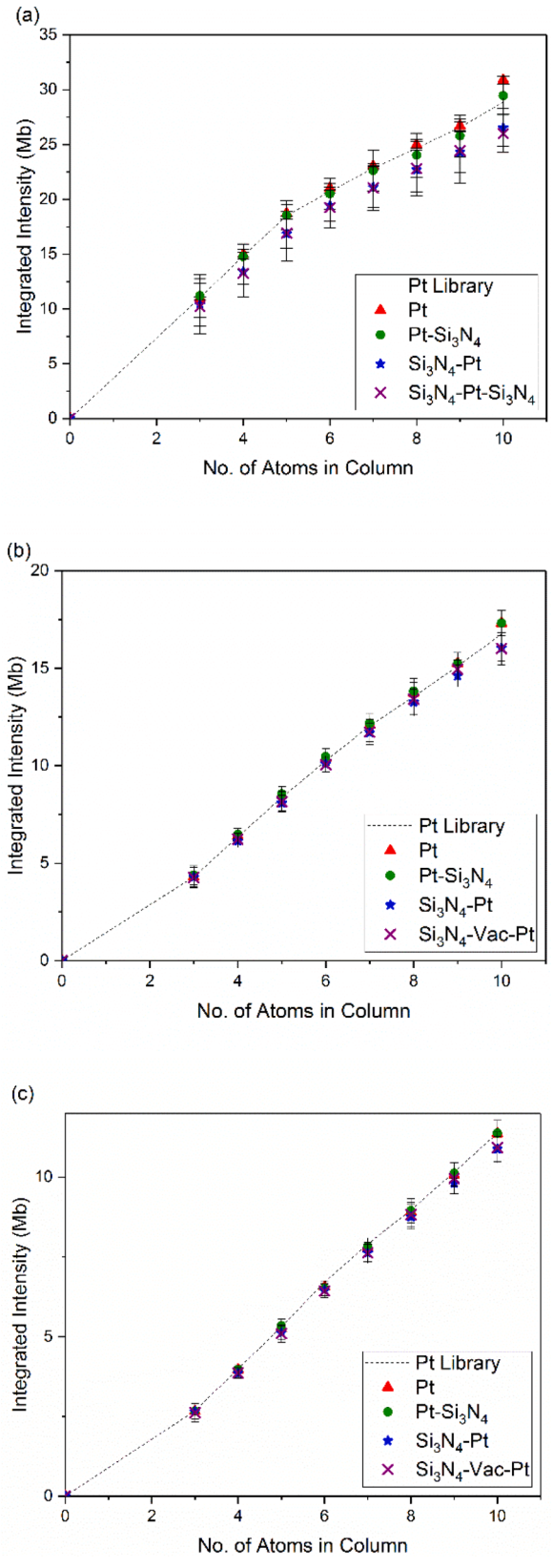

Figure 5. Individual scattering cross sections for each atomic column in simulations of the Pt nanoparticle compared with library values for pure Pt for (a) 80, (b) 200 and (c) 300 kV. Error bars represent single standard deviations from columns of the same thickness.

the integrated Pt cross-sections are further from the Pt reference library, suggesting that a higher accelerating voltage is preferable for MEMS-based experiments, presumably as a consequence of decreased scattering in the Si_3N_4 membrane. For all three accelerating voltages, the Si_3N_4-Pt simulation shows a reduction in atomic column intensity, most likely because the Si_3N_4 scatters the electron beam, meaning that less of it reaches the nanoparticle. The Si_3N_4-Vac-Pt simulation, in which there is a 2 nm gap between the membrane and the nanoparticle, was used to determine whether a greater distance between the nanoparticle and the membrane reduces the influence of the membrane on quantification. Although the 2 nm gap produces little change in the intensities, in a real experimental setup the distance between the chips is typically 5-30 μm and the effect of the top membrane may be smaller due to the material being further from focus.

A small variation between different columns of the same thickness is seen in the simulations as a result of the presence of different nearest neighbours [32]. As an absolute value, this variation generally increases with sample thickness. However, as a percentage standard deviation it stays approximately constant, as shown in Fig. 6. Its value is approximately 1% at 200 and 300 kV, but closer to 1.5% at 80 kV. The presence of a Si_3N_4 membrane (either above or below the nanoparticle) increases the standard deviation for the 3-atom-thick columns due to the increased variation in integration area. For other atomic columns, the average standard deviations are 8%, 4% and 3.7% at 80, 200 and 300 kV, respectively. For a 6-atom-thick column, these values are equivalent to counting errors of ±1.45, ±0.44 and ±0.37 atoms, demonstrating that in the absence of statistical (shot) noise and other artefacts single atom sensitivity is in principle possible at 200 and 300 kV, but not at 80 kV. Although the variation in cross section between different atomic columns that have the same thickness results in part from the presence of different numbers of neighbouring columns, Fig. 6 shows that it accounts for less than 25% of the total variation seen in the supported nanoparticle simulations.

Simulations with Si_3N_4 both above and below the nanoparticle were performed at 200 kV. The values are slightly higher than for the simulated reference library, but are still mostly within 5% of the library values and increase monotonically with thickness, as shown in Fig. 7. It should be noted that statistical methods, such as those of van Aert, are applicable so long as the values increase monotonically with thickness, even if they deviate from simulated library values.

Two different approaches, which are summarised in Tables 1 and 2, can be used to determine the accuracy of ADF STEM quantification based on the above simulations. A full detailed error analysis broken down by accelerating voltage and sample thickness is presented in the Supplementary Information.

In the first approach, which is summarised in Table 1, the measured cross section values are compared with those from a reference library, as described above. The standard deviation is then either added to or subtracted from the average intensity and the resulting atom number assignment is determined. In this way, it is possible to evaluate the accuracy of atom counting based on a direct comparison between experimental results and simulations. In Table 1, the counting accuracies of the model structures are compared for different accelerating voltages and show up to which number of atoms within a column a counting accuracy of + or – 1 atom can be achieved. If the value is outside the investigated range (3-10 atoms) then "<3" or ">10" is written. "<3" indicates that single atom counting accuracy is not possible, even for the smallest simulated thickness. ">10" indicates that single atom counting accuracy is possible over the full investigated range. The results show that at 80 kV the best possible -1 atom counting accuracy can be achieved for Pt-Si_3N_4. In contrast, for Si_3N_4-Pt and Si_3N_4-Vac-Pt an atom counting accuracy of -1 atom is not possible, other than for below 4 atoms, while an accuracy of +1 atom or better is possible up to at least 10 atoms. This asymmetry in the atom counting error could lead to a systematic underestimation in atom counting analysis for Si_3N_4-Pt and Si_3N_4-Vac-Pt. At 200 kV, single atom sensitivity is possible for Pt-Si_3N_4

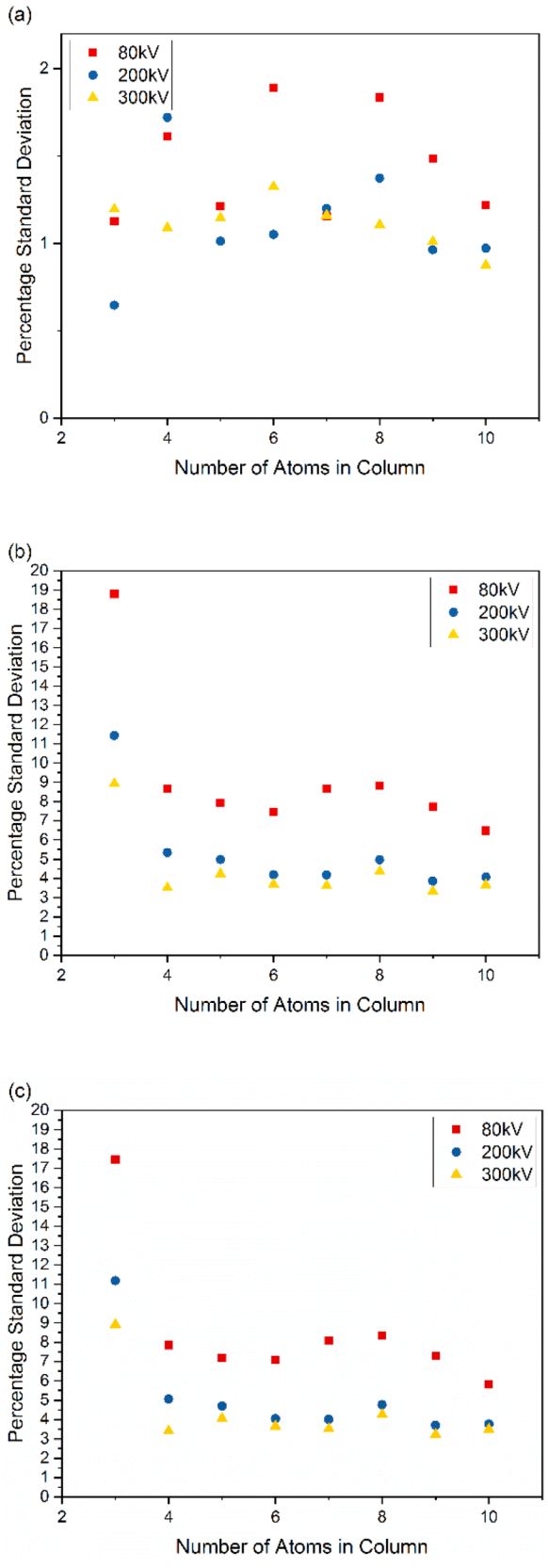

Figure 6. Comparison of percentage standard deviation in integrated cross section between atomic columns of the same thickness for (a) the Pt nanoparticle alone; (b) the Pt nanoparticle with Si_3N_4 below it; (c) the Pt nanoparticle with Si_3N_4 above it.

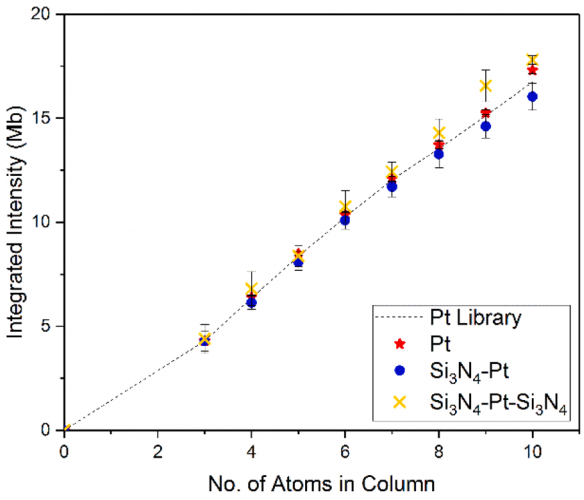

Figure 7. Comparison of integrated cross sections for columns of different thickness for simulations with Si_3N_4 membranes both above and below the Pt nanoparticle.

Table 1
Summary of atom counting limitations for direct comparisons with simulations for different model structures and accelerating voltages. Each column shows the thickness above which the average simulated value after subtracting or adding the standard deviation would result in an atom counting assignment of -1 or +1 from the true value.

	Pt-Si_3N_4		Si_3N_4-Pt		Si_3N_4-Vac-Pt		Si_3N_4-Pt- Si_3N_4	
	-1	+1	-1	+1	-1	+1	-1	+1
80kV	6	<3	<3	>10	4	>10	-	-
200kV	>10	8	8	>10	8	>10	9	7
300kV	>10	10	8	>10	8	>10	-	-

Table 2
Summary of atom counting limitations for a statistical quantification method for different model structures and accelerating voltages. Each column shows the thickness above which an error of ±0.5 (or ±1) atoms would occur.

	Pt-Si_3N_4		Si_3N_4-Pt		Si_3N_4-Vac-Pt		Si_3N_4-Pt- Si_3N_4	
	±0.5	±1	±0.5	±1	±0.5	±1	±0.5	±1
80kV	<3	6	<3	6	<3	<3	-	-
200kV	7	>10	7	>10	7	>10	4	-
300kV	8	>10	8	>10	7	>10	-	-

and Si_3N_4-Pt up to a thickness of 8 atoms. For greater numbers of atoms, the accuracy decreases with increasing sample thickness. For the Si_3N_4-Pt-Si_3N_4 simulations, single atom sensitivity only persists up to a thickness of 7 atoms, decreasing to +1/-0 atoms for greater thicknesses. This asymmetry would result in a systematic over-estimation in the number of atom counts. At 300 kV, single atom sensitivity persists up to the full thickness of 10 atoms for the Pt-Si_3N_4 simulation and up to 8 atoms for the Si_3N_4-Pt and Pt-Vac- Si_3N_4 simulations.

In the second approach, which is summarised in Table 2, the standard deviation is compared with half of the distance between the mean intensities of columns. This is comparable to the degree of overlap that might be found during Gaussian fitting using the statistical method. At 80 kV, the outlook is rather poor, as an accuracy of +/-1 atom is only possible up to a thickness of 6 atoms for Pt-Si_3N_4, while for the other structures it is less than 3 atoms. At 200 kV, the accuracy is better than +/-0.5 atom for the Pt-Si_3N_4 and Si_3N_4-Pt simulations up to a thickness of 8 atoms. For the Si_3N_4-Pt-Si_3N_4 simulation, the accuracy is +/- 0.6-0.8 atoms even at the maximum thickness investigated. At 300 kV, an accuracy of +/-0.5 atoms is possible up to a thickness of 4 atoms, but reduces marginally to a maximum of +/- 0.7 atoms at the largest thickness

of 10 atoms.

In summary, single atom counting accuracy is generally not achievable at 80kV. Atom counting improves with increasing accelerating voltage. Single atom counting accuracy is attainable at 200 and 300 kV and is is slightly improved at 300 kV compared with 200 kV. The presence of a systematic bias means that direct comparisons between experimental results and simulations should be applied with caution. The simulations that are used for the reference library should necessarily include the effects of the membrane. A statistical-based atom counting method could be applied with little to no modification to the approach.

All of the simulations that are presented here are based on stoichiometric Si_3N_4 with a thickness of 20 nm. It is safe to assume that the effects that we observe will be greater with increasing membrane thickness. The theoretical maximum atom counting accuracies discussed above will be reduced by the presence of additional experimental errors; including scanning distortions and noise. Scanning distortions can affect the measured intensities and therefore the resulting atom assignment, which is also seen as a broadening of histograms, which affects statistical methods [53]. Non-rigid registration of a time series of images has been shown to reduce such effects [46,54]. Likewise, noise effects will be minimised by using the highest dose that the sample allows, possibly accumulating counts over several frames to keep the dose rate low.

4. Conclusions

In this paper, simulations have been used to assess the influence of the presence of SiN_x membranes on the quantification of atomic-resolution ADF STEM images of Pt nanoparticles. Density variations within the membrane and additional scattering of the electron beam are shown to affect the final measured intensities for each atomic column, resulting in errors in any subsequent atom counting measurements. For the three accelerating voltages studied, the most significant effect on the accuracy of atom counting for Pt nanoparticles is observed at 80 kV, when the scattering contribution from SiN_x is greatest. The best accuracy attainable is then +/-1 atom, although this value will be reduced in the presence of other experimental errors. At 200 and 300 kV, the influence of the SiN_x membrane is smaller and errors in atom counting are lower. Out of these two accelerating voltages, 300 kV provides slightly better accuracy. If the membrane is above the Pt nanoparticle, then (background-subtracted) cross-sections are lower than comparison library values for a Pt nanoparticle in the absence of supporting SiN_x. This difference may result from the fact that a ́dirty ́ beam, which has been pre-scattered by a SiN_x membrane, has a lower intensity before it interacts with each Pt column. However, this error is small at the thicknesses considered here (up to 10 atoms, or 2.4nm) and single atom sensitivity in atom counting accuracy can still in principle be achieved. Although the accuracy of atom counting is lower at larger specimen thicknesses, if the signal remains monotonic with thickness then a statistical method may be more robust for such an analysis.

Declaration of Competing Interest

The authors have no competing conflicts of interest to declare.

Acknowledgments

K. E. MacArthur and M. Heggen acknowledge the Helmholtz Association and the DFG (grant number HE 7192/1-2) for financial support of this work.

References

[1] P.L. Hansen, J.B. Wagner, S. Helveg, J.R. Rostrup-Nielsen, B.S. Clausen, H. Topsøe, Atom-resolved imaging of dynamic shape changes in supported copper nanocrystals, Science (80-.) 295 (2002) 2053–2055, https://doi.org/10.1126/science.1069325.

[2] R. Farra, J. Cao, A. Rinaldi, Z.-J. Wang, E. Willinger, X. Huang, et al., Multi-Scale Red-Ox Dynamics of Active Metal Catalysts Revealed by a Combination of In Situ Scanning and Transmission Electron Microscopy, Microsc. Microanal. 23 (2017) 922–923, https://doi.org/10.1017/s143192761700527x.

[3] P. Abellan, S. Mehraeen, P. Xu, J.T. McKeown, P.V. Deshmukh, J.E. Evans, et al., High gas pressure /high temperature in situ investigation of nanomaterials by STEM-EELS, Microsc. Microanal. 18 (2012) 1170–1171, https://doi.org/10.1017/S1431927612007702.

[4] N.J. Zaluzec, When is Si3N4 not Si3N4? When it is a Low Stress SiNx Membrane Window, Microsc. Microanal. 21 (2015) 959–960, https://doi.org/10.1017/s1431927615005590.

[5] P.L. Gai, Developments in in situ environmental cell high-resolution electron microscopy and applications to catalysis, Top. Catal. 21 (2002) 161–173, https://doi.org/10.1023/A:1021333310817.

[6] A.T. DeLaRiva, T.W. Hansen, S.R. Challa, A.K. Datye, In situ Transmission Electron Microscopy of catalyst sintering, J. Catal. 308 (2013) 291–305, https://doi.org/10.1016/j.jcat.2013.08.018.

[7] S. Van Aert, K.J. Batenburg, M.D. Rossell, R. Erni, G. Van Tendeloo, Three-Dimensional Atomic Imaging of Crystalline Nanoparticles, Nature 470 (2011) 374–377, https://doi.org/10.1038/nature09741.

[8] S. Bals, M. Casavola, M.A. van Huis, S. Van Aert, K.J. Batenburg, G. Van Tendeloo, et al., Three-Dimensional Atomic Imaging of Colloidal Core-Shell Nanocrystals, Nano Lett 11 (2011) 3420–3424, https://doi.org/10.1021/nl201826e.

[9] K.J. Batenburg, S. Bals, J. Sijbers, C. Kübel, P.A. Midgley, J.C. Hernandez, et al., 3D Imaging of Nanomaterials by Discrete Tomography, Ultramicroscopy. 109 (2009) 730–740, https://doi.org/10.1016/j.ultramic.2009.01.009.

[10] A. Skorikov, W. Albrecht, E. Bladt, X. Xie, J.E.S. Van Der Hoeven, A. Van Blaaderen, et al., Quantitative 3D Characterization of Elemental Diffusion Dynamics in Individual Ag@Au Nanoparticles with Different Shapes, ACS Nano. 13 (2019) 13421–13429, https://doi.org/10.1021/acsnano.9b06848.

[11] L. Jones, K.E. MacArthur, V.T. Fauske, A.T.J. van Helvoort, P.D. Nellist, Rapid estimation of catalyst nanoparticle morphology and atomic-coordination by high-resolution z-contrast electron microscopy, Nano Lett 14 (2014) 6336–6341, https://doi.org/10.1021/nl502762m.

[12] K.E. MacArthur, L. Jones, D. Ozkaya, S. Lozano-Perez, P.D. Nellist, Quantification of PtIr Catalyst Nanoparticles using ADF STEM, 18th Int. Microsc. Congr. MS-1-P-222, 2014.

[13] J. Aarons, L. Jones, A. Varambhia, K.E. MacArthur, D. Ozkaya, M. Sarwar, et al., Predicting the Oxygen-Binding Properties of Platinum Nanoparticle Ensembles by Combining High-Precision Electron Microscopy and Density Functional Theory, Nano Lett 17 (2017) 4003–4012, https://doi.org/10.1021/acs.nanolett.6b04799.

[14] A. Singhal, J.C. Yang, J.M. Gibson, STEM-based mass spectroscopy of supported Re clusters, Ultramicroscopy 67 (1997) 191–206, https://doi.org/10.1016/S0304-3991(96)00094-0.

[15] A. Rosenauer, K. Gries, K. Müller-Caspary, A. Pretorius, M. Schowalter, A. Avramescu, et al., Measurement of specimen thickness and composition in Al(x)Ga(1-x)N/GaN using high-angle annular dark field images, Ultramicroscopy 109 (2009) 1171–1182, https://doi.org/10.1016/j.ultramic.2009.05.003.

[16] S.D. Findlay, J.M. LeBeau, Detector Non-Uniformity in Scanning Transmission Electron Microscopy, Ultramicroscopy 124 (2013) 52–60, https://doi.org/10.1016/j.ultramic.2012.09.001.

[17] K.E. MacArthur, L. Jones, P.D. Nellist, How flat is your detector? Non-uniform annular detector sensitivity in STEM quantification, J. Phys. Conf. Ser. 522 (2014), 012018, https://doi.org/10.1088/1742-6596/522/1/012018.

[18] G.T. Martinez, L. Jones, A. De Backer, A. Béché, J. Verbeeck, S. Van Aert, et al., Quantitative STEM normalisation: The importance of the electron flux, Ultramicroscopy 159 (2015) 46–58, https://doi.org/10.1016/j.ultramic.2015.07.010.

[19] J.M. LeBeau, S.D. Findlay, L.J. Allen, S. Stemmer, Standardless atom counting in scanning transmission electron microscopy, Nano Lett 10 (2010) 4405–4408, https://doi.org/10.1021/nl102025s.

[20] S. Van Aert, A. De Backer, G.T. Martinez, B. Goris, S. Bals, G. Van Tendeloo, et al., Procedure to count atoms with trustworthy single-atom sensitivity, Phys. Rev. B. 87 (2013), 064107, https://doi.org/10.1103/PhysRevB.87.064107.

[21] T. Altantzis, I. Lobato, A. De Backer, A. Béché, Y. Zhang, S. Basak, et al., Three-Dimensional Quantification of the Facet Evolution of Pt Nanoparticles in a Variable Gaseous Environment, Nano Lett 19 (2019) 477–481, https://doi.org/10.1021/acs.nanolett.8b04303.

[22] A. De wael, A. De Backer, L. Jones, P.D. Nellist, S. Van Aert, Hybrid statistics-simulations based method for atom-counting from ADF STEM images, Ultramicroscopy (2017), https://doi.org/10.1016/j.ultramic.2017.01.010.

[23] A. De Backer, G.T. Martinez, A. Rosenauer, S. Van Aert, Atom counting in HAADF STEM using a statistical model-based approach: methodology, possibilities, and inherent limitations, Ultramicroscopy 134 (2013) 23–33, https://doi.org/10.1016/j.ultramic.2013.05.003.

[24] A.M. Varambhia, L. Jones, A. De Backer, V.T. Fauske, S. Van Aert, D. Ozkaya, et al., Quantifying a Heterogeneous Ru Catalyst on Carbon Black Using ADF STEM, Part. Part. Syst. Charact. 33 (2016) 438–444, https://doi.org/10.1002/ppsc.201600067.

[25] H. Katz-Boon, C.J. Rossouw, C. Dwyer, J. Etheridge, Rapid measurement of nanoparticle thickness profiles, Ultramicroscopy 124 (2013) 61–70, https://doi.org/10.1016/j.ultramic.2012.08.009.

[26] A. Rosenauer, K. Gries, K. Müller-Caspary, M. Schowalter, A. Pretorius, A. Avramescu, et al., Measurement of composition profiles in III-nitrides by quantitative scanning transmission electron microscopy, J. Phys. Conf. Ser. 209 (2010), 012009, https://doi.org/10.1088/1742-6596/209/1/012009.

[27] R. Fritz, A. Beyer, W. Stolz, K. Müller-Caspary, M. Schowalter, A. Rosenauer, et al., Quantitative Analysis of Chemical Composition Using HAADF-STEM in a JEOL 2200FS, Microsc. Microanal. 17 (2011) 1410–1411, https://doi.org/10.1017/S1431927611007926.
[28] T. Grieb, K. Müller-Caspary, R. Fritz, M. Schowalter, N. Neugebohrn, N. Knaub, et al., Determination of the chemical composition of GaNAs using STEM HAADF imaging and STEM strain state analysis, Ultramicroscopy 117 (2012) 15–23, https://doi.org/10.1016/j.ultramic.2012.03.014.
[29] E. Carlino, V. Grillo, Atomic-resolution quantitative composition analysis using scanning transmission electron microscopy Z-contrast experiments, Phys. Rev. B. 71 (2005) 1–8, https://doi.org/10.1103/PhysRevB.71.235303.
[30] E. Rotunno, M. Albrecht, T. Markurt, T. Remmele, V. Grillo, Three dimensional analysis of the composition in solid alloys by variable probe in scanning transmission electron microscopy, Ultramicroscopy 146 (2014) 62–70, https://doi.org/10.1016/j.ultramic.2014.07.003.
[31] G.T. Martinez, A. Rosenauer, A. De Backer, J. Verbeeck, S. Van Aert, Quantitative composition determination at the atomic level using model-based high-angle annular dark field scanning transmission electron microscopy, Ultramicroscopy 137 (2014) 12–19, https://doi.org/10.1016/j.ultramic.2013.11.001.
[32] H. E, K.E. MacArthur, T.J. Pennycook, E. Okunishi, A.J. D'Alfonso, N.R. Lugg, et al., Probe integrated scattering cross sections in the analysis of atomic resolution HAADF STEM images, Ultramicroscopy 133 (2013) 109–119, https://doi.org/10.1016/j.ultramic.2013.07.002.
[33] K.E. MacArthur, A.J. D'Alfonso, D. Ozkaya, L.J. Allen, P.D. Nellist, Optimal ADF STEM imaging parameters for tilt-robust image quantification, Ultramicroscopy 156 (2015) 1–8, https://doi.org/10.1016/j.ultramic.2015.04.010.
[34] G.T. Martinez, A. De Backer, A. Rosenauer, J. Verbeeck, S. Van Aert, The effect of probe inaccuracies on the quantitative model-based analysis of high angle annular dark field scanning transmission electron microscopy images, Micron. 63 (2014) 57–63. doi:10.1016/j.micron.2013.12.009.
[35] R. Brydson, Aberration-Corrected Analytical Transmission Electron Microscopy, Wiley, 2011. https://books.google.de/books?id=ZL602A70T2UC.
[36] A. De Backer, G.T.G.T. Martinez, K.E.K.E. Macarthur, L. Jones, A. Béché, P.D.P. D. Nellist, et al., Dose limited reliability of quantitative annular dark field scanning transmission electron microscopy for nano-particle atom-counting, Ultramicroscopy 151 (2015) 56–61, https://doi.org/10.1016/j.ultramic.2014.11.028.
[37] S. Van Aert, A. De Backer, A. De wael, L. Jones, G.T. Martinez, B. Goris, et al., Non-destructive nanoparticle characterisation using a minimum electron dose in quantitative ADF STEM: how low can one go? Eur. Microsc. Congr. (2016) 509–510, https://doi.org/10.1002/9783527808465.EMC2016.6196, 2016 ***Proc***.
[38] A. De wael, A. De Backer, L. Jones, A. Varambhia, P.D. Nellist, S. Van Aert, Measuring Dynamic Structural Changes of Nanoparticles at the Atomic Scale Using Scanning Transmission Electron Microscopy, Phys. Rev. Lett. 124 (2020), 106105, https://doi.org/10.1103/PhysRevLett.124.106105.
[39] J.K. Nørskov, J. Rossmeisl, A. Logadottir, L. Lindqvist, J.R. Kitchin, T. Bligaard, et al., Origin of the overpotential for oxygen reduction at a fuel-cell cathode, J. Phys. Chem. B. 108 (2004) 17886–17892, https://doi.org/10.1021/jp047349j.
[40] Nenad M. Markovic, H.A. Gasteiger, P.N. Ross, Oxygen Reduction on Platinum Low-Index Single-Crystal Surfaces in Sulfuric Acid Solution: Rotating Ring-Pt(hkZ) Disk Studies, J. Phys. Chem. 99 (1995) 3411, https://doi.org/10.1021/j100011a001.
[41] A. Surrey, L. Schultz, B. Rellinghaus, Multislice simulations for in-situ HRTEM studies of nanostructured magnesium hydride at ambient hydrogen pressure, Ultramicroscopy 175 (2017) 111–115, https://doi.org/10.1016/j.ultramic.2017.01.017.
[42] C.B. Boothroyd, Quantification of high-resolution electron microscope images of amorphous carbon, Ultramicroscopy 83 (2000) 159–168, https://doi.org/10.1016/S0304-3991(00)00012-7.
[43] L.J. Allen, T.W. Josefsson, Inelastic Scattering of Fast Electrons by Crystals, Phys. Rev. B. Condens. Matter. 52 (1995) 3184–3198. http://www.ncbi.nlm.nih.gov/pubmed/17303621.
[44] W. Van den Broek, X. Jiang, C.T. Koch, FDES, a GPU-based multislice algorithm with increased efficiency of the computation of the projected potential, Ultramicroscopy 158 (2015) 89–97, https://doi.org/10.1016/j.ultramic.2015.07.005.
[45] H.X. Gao, L.-M. Peng, Parameterization of the temperature dependence of the Debye–Waller factors, Acta Crystallogr. Sect. A Found. Crystallogr. 55 (1999) 926–932, https://doi.org/10.1107/S0108767399005176.
[46] M. Nord, P.E. Vullum, I. MacLaren, T. Tybell, R. Holmestad, Atomap: a new software tool for the automated analysis of atomic resolution images using two-dimensional Gaussian fitting, Adv. Struct. Chem. Imaging. 3 (2017) 9, https://doi.org/10.1186/s40679-017-0042-5.
[47] F. de la Pena, T. Ostasevicius, V. Tonaas Fauske, P. Burdet, P. Jokubauskas, M. Nord, et al., Electron Microscopy (Big and Small) Data Analysis With the Open Source Software Package HyperSpy, Microsc. Microanal. 23 (2017) 214–215, https://doi.org/10.1017/S1431927617001751.
[48] A. Rosenauer, T. Mehrtens, K. Müller-Caspary, K. Gries, M. Schowalter, P. V. Satyam, et al., Composition mapping in InGaN by scanning transmission electron microscopy, Ultramicroscopy 111 (2011) 1316–1327, https://doi.org/10.1016/j.ultramic.2011.04.009.
[49] D.T. Nguyen, S.D. Findlay, J. Etheridge, The spatial coherence function in scanning transmission electron microscopy and spectroscopy, Ultramicroscopy 146 (2014) 6–16, https://doi.org/10.1016/j.ultramic.2014.04.008.
[50] Y.-G. So, K. Kimoto, Effect of specimen misalignment on local structure analysis using annular dark-field imaging, J. Electron Microsc. (Tokyo). 61 (2012) 207–215, https://doi.org/10.1093/jmicro/dfs045.
[51] D. Reem, The geometric stability of voronoi diagrams with respect to small changes of the sites. Proc. 27th Annu. ACM Symp. Comput. Geom. - SoCG '11, ACM Press, New York, New York, USA, 2011, p. 254, https://doi.org/10.1145/1998196.1998234.
[52] K.E. MacArthur, H.G. Brown, S.D. Findlay, L.J. Allen, Probing the effect of electron channelling on atomic resolution energy dispersive X-ray quantification, Ultramicroscopy 182 (2017) 264–275, https://doi.org/10.1016/j.ultramic.2017.07.020.
[53] L. Jones, H. Yang, T.J. Pennycook, M.S.J. Marshall, S. Van Aert, N.D. Browning, et al., Smart Align—a new tool for robust non-rigid registration of scanning microscope data, Adv. Struct. Chem. Imaging. 1 (2015) 8, https://doi.org/10.1186/s40679-015-0008-4.
[54] A.B. Yankovich, B. Berkels, W. Dahmen, P. Binev, S.I. Sanchez, S. Bradley, et al., Picometre-precision analysis of scanning transmission electron microscopy images of platinum nanocatalysts, Nat. Commun. 5 (2014) 4155, https://doi.org/10.1038/ncomms5155.